PCCP

Accepted Manuscript




ROYAL SOCIETY OF CHEMISTRY

www.rsc.org/pccp

# Molecular Dynamics Simulations of Proton–Ordered Water Confined in Low-Diameter Carbon Nanotubes

Shujuan Li and Burkhard Schmidt

*Institute for Mathematics, Freie Universität Berlin*

*Arnimallee 6, D-14195 Berlin, Germany*

(Dated: February 4, 2015)

## Abstract

The present work deals with molecular dynamics simulations of water confined in single–walled carbon nanotubes (CNTs), with emphasis on the proton-ordering of water and its polarization. First, the water occupancy of open–ended armchair and zigzag CNTs immersed in water under ambient $NPT$ conditions is calculated for various water models, and for varying Lennard–Jones parameters of the water–carbon interaction. As a function of the CNT diameter, the water density displays several oscillations before converging to the bulk value.

Based on these results, the water structures encapsulated in 10 nm long armchair CNTs $(n, n)$ with $5 \leq n \leq 10$, are investigated under $NVT$ conditions. Inside the smallest nanotubes ($n = 5, 6$) highly ferroelectric (FE), quasi–one–dimensional water chains are found while inside the other CNTs water molecules assemble into single–walled ice nanotubes (INTs). There are several, near–degenerate minimum energy INT structures: Single helical structures were found for $7 \leq n \leq 10$, in all cases in FE arrangement. In addition, a double helical INT structure was found for $n = 8$ with an even higher polarization. Prism–like structure were found only for $8 \leq n \leq 10$ with various FE, ferrielectric (FI), and antiferroelectric (AF, $n = 9, 10$) proton ordering.

The coexistence of the nearly iso-energetic FE, FI, and AF INT structures separated by high barriers renders the molecular dynamics highly metastable, typically with nanosecond timescales at room temperature. Hence, the replica exchange simulation method is used to obtain populations of different INT states at finite temperatures. Many of the FE INT structures confined in low–diameter CNTs are still prevalent at room temperature. Both helix–helix and helix–prism structural transitions are detected which can be either continuous (around 470 K for $n = 8$) or discontinuous (at 218 K for $n = 9$). Also melting–like transitions are found in which the INT structures are disrupted leading to a loss of FE or FI ordering of the water orientations. Also these transitions can be either smooth (for $n = 7, 8$) or abrupt, first–order transitions, at $T = 362$ K for $n = 9$ and at $T = 285$ K for $n = 10$.

## I. INTRODUCTION

All known phases of ice obey the Bernal–Fowler rules which require that each water molecule is involved in tetrahedral hydrogen bonding, donating two protons from adjacent water molecules while accepting two protons from other neighbors [1]. This rule, however, leaves many different, nearly degenerate orientations of the individual water molecules. In particular, one question has attracted a lot of attention for many years [2–4]: Can ice be ferroelectric (FE), i. e., can all molecular dipoles be oriented in the same direction, resulting in a huge net polarization? Already in the 1930s, Bernal and Fowler suggested that the water molecules of hexagonal ice $I_h$ can adopt such a proton-ordered arrangement [1]. However, only little later Pauling argued that the number of ice structures compatible with the Bernal–Fowler rules is proportional to $(3/2)^{N_W}$ where $N_W$ is the number of water molecules [5]. This renders the existence of FE ice practically impossible, whereas in almost all other arrangements the molecular dipoles do not follow regular patterns, thus canceling out the polarization. Indeed, Pauling's theory was verified by calorimetric measurements [6], by neutron scattering studies [7, 8] and by depolarization measurements [9].

While there is no report about the existence of FE ice under natural conditions on earth, it is under debate whether proton ordered ice exists in the outer solar system [10, 11]. In laboratory, micro-domains of ferroelectric ice can be obtained by doping ice with hydroxides [12–16] or acids [17, 18] acting as catalyzers. Based on simulation studies, also the freezing of supercooled water in the presence of static electric fields has been suggested to generate FE water [19]. Alternatively, proton–ordering can be induced in environments of effectively reduced dimensionality: Quasi–two–dimensional, thin ferroelectric ice layers can be grown on platinum surfaces [20, 21] or can be found in hydration shells around proteins [22]. Quasi–one–dimensional proton ordered water structures have been found in specific supramolecular structures [23] or in trenches of kaolinite mineral [24].

In this paper, we study the ferroelectric properties of water confined inside single–walled carbon nanotubes (CNTs) of low diameter $d$. In recent years the structure and dynamics of these systems have received a lot of attention [25–40]. The smallest CNTs with $d$ between 0.7 and 0.8 nm can accommodate quasi–one–dimensional water wires held together by hydrogen-bonds and which are known to be FE. Slightly larger CNTs with $d$ between 1 and 1.5 nm may accomodate single–walled ice nanotubes (INTs) which can be either prism–like (polygonal

rings of water stacked along the CNT axis) or helical, both of which fulfill the Bernard–Fowler rules of fourfold coordination of water. Note that all of these structures can be considered as exotic ice phases not present in bulk water.

Similar to the case of bulk ice, also in INTs the water molecules can assume different types of proton ordering [37]. In close analogy to definitions in magnetism they are referred to as ferroelectric, antiferroelectric and ferrielectric throughout this work. In ferroelectric (FE) water all dipole moments are collectively oriented, contributing to a net polarization. In antiferroelectric (AF) water, the dipole moments are also aligned but with opposing orientation, with dipole moments of neighboring water molecules (here between neighboring prism edges) pointing in opposite direction, leading to zero polarization. In ferrielectric (FI) water, the opposing moments are unequal and hence yield a non-zero polarization. The existence of these proton–ordering schemes in water confined in small CNTs, has been investigated recently by means of molecular dynamics simulations. It was indeed found that FE, FI, and AF INT structures can exist with single domains extending over lengths of several nanometers [41, 42]. In subsequent work it was found that the proton–ordering of water inside CNTs can prevail even under ambient conditions, see Ref. [43–45]. In those works, also the question of metastability of various INT structures was encountered, and it was found that transitions between INT structures of different polarization can be considered as rare events, occuring on a timescale of nanoseconds or even beyond. Clearly, this slow dynamics is due to the geometric frustrations imposed by the INT structures where single water molecules cannot reorient without many (or even all) of their neighbors also reorienting, thus resulting in high energetic barriers. Similar findings were also made for CNT confined INTs in the presence of external electrostatic fields [46].

Motivated by these findings the present work aims at a systematic study of proton ordering of water confined in low–diameter CNTs. In particular there are three issues which shall be addressed here: Based on a force field determined previously by fitting to high–level quantum chemistry calculations [47], see Sec. II A, we first simulate the spontaneous water filling of open–ended CNTs immersed in water, see Sec. II B. For a variety of armchair and zigzag CNTs, the resulting densities of water confined in CNTs are discussed in Sec. III A. Once the water occupancies have been determined, the second part of this work deals with different minimum energy INT structures. For the case of armchair CNTs $(n, n), 5 \leq n \leq 10$ we give in Sec. III B an overview of INT structures and characterize

them in terms of their energetics as well as their proton ordering schemes and the resulting polarization, thus classifying them as FE, FI, or AF water. In the third part, finite temperature effects on structure and dynamics of INTs confined in CNTs are considered. Because of the mentioned metastable behavior of near–degenerate INT structures separated by relatively high barriers, the ergodic assumption underlying conventional MD simulations may not be fulfilled. Consequently, we resort here to the replica-exchange molecular dynamics (REMD) method [48–52]. By swapping between different temperatures, which are simulated in parallel, REMD simulations can overcome barriers between local minima, see Sec. II C. This technique will not only be instrumental in calculating the populations of various INT structures as a function of temperature but it also allows us to find structural transitions when varying the temperature. As will be shown in Sec. III C, INTs exhibit different types of such transitions which can be either continuous or abrupt, in the latter case resembling first–order phase transitions with corresponding latent heats.

## II. SIMULATION METHODS

### A. Water–Carbon Force Field

In this work the approximation of pairwise additive, empirical Lennard-Jones (LJ) potential energy functions is used to model the non-bonded interaction energy

$$V(r_{ij}) = 4\sum_{i<j}\epsilon_{ij}\left[\left(\frac{\sigma_{ij}}{r_{ij}}\right)^{12} - \left(\frac{\sigma_{ij}}{r_{ij}}\right)^{6}\right] \tag{1}$$

where the summation extends over all atoms ($i$) of the water molecules and all atoms ($j$) in the CNTs, at distance $r_{ij}$, with collision diameters $\sigma_{ij}$ and well depths $\epsilon_{ij}$. For the specific case of water–carbon interactions, we define the overall interaction strength $\eta$ and the anisotropy parameter $\delta$ [47]

$$\begin{aligned}\eta &= \epsilon_{CO} + 2\epsilon_{CH} \\ \delta &= 1 - (\epsilon_{CO} - 2\epsilon_{CH})/\eta\end{aligned} \tag{2}$$

While most previous simulations of water inside CNT had been based on empirical values for the LJ parameters, we reparametrized in our earlier work [47] the water–carbon interaction by fitting to CCSD(T) high level quantum chemical calculations for the water–graphene

interaction [53]. This yielded a stronger water–carbon interaction, $\eta$ =1 kJ/mol, than in most of the previous work [25, 54–56]. In addition, our water–carbon interaction is notably anisotropic with $\delta \approx 1$, unlike most of the previous simulations which assumed an isotropic water–carbon interaction, $\delta = 0$. This anisotropy is based on the difference in the interaction of graphene with water with the hydrogen atoms pointing up or down [53]. Similar results ($\eta > 1$ kJ/mol, $\delta > 1$ were also found on the basis of vdW-DFT calculations of water outside CNTs [57]. Finally, our fit to the quantum chemical calculations resulted in $\sigma_{CO}$ =315.7 pm and $\sigma_{CH}$ =272.6 pm, in close agreement with values in most of the literature and which are very close to the corresponding van der Waals values of 322 pm and 272 pm [58].

### B. MD simulations of Open CNTs Immersed in Water

We first determine how many water molecules spontaneously enter various open-ended armchair and zigzag CNTs immersed in water. This number, $N_W$, is obtained from molecular dynamics (MD) simulations of CNTs dissolved in water with a given temperature and pressure. Assuming a constant carbon–carbon bond length $a = 141.8$ pm, the length of the armchair CNTs $(n, n)$ is 10.07 nm (41 unit cells of $\sqrt{3}a = 245.6$ pm each), whereas the length of the zigzag CNTs $(n, 0)$ is 10.21 nm (24 unit cells of $3a = 425.6$ pm each). Nine different CNTs were investigated simultaneously in one (periodic) simulation box of $14 \times 14 \times 20$ nm$^3$ which is large enough to safely neglect interaction between the CNTs.

The MD-simulations were carried out using the GROMACS 4.5 software package [59] within the $NPT$ ensemble. The water–water interaction is modeled in terms of three–particle rigid models SPC [60], SPCE [61], TIP3P[62], four–particle rigid model TIP4P [62], and five–particle rigid model TIP5P [63]. The water molecules and the CNTs are assumed to interact through the Lennard-Jones potential energy function introduced in Sec. II A. The CNTs are kept frozen during these simulations and the internal coordinates of water molecules are constrained by the SETTLE algorithm [64]. The duration of the simulations is 10 ns with an initial equilibration period of 1 ns. The temperature $T = 300$ K is controlled by the velocity-rescaling thermostat with a coupling constant $\tau = 0.2$ ps [65] and the pressure $P = 10^5$ Pa is controlled by the pressure coupling Berendsen barostat [66] which is isotropic in X, Y and Z direction. The equations of motion are integrated using the leap-frog algorithm with a timestep of 1 fs with periodic boundary conditions in all

directions. For the LJ part of the water–water interaction a cutoff radius 0.9 nm is applied while the Coulombic part is treated by a real-space cutoff at 0.9 nm and the reciprocal part is described by the particle–mesh Ewald (PME) method [67, 68].

### C. REMD simulations of Water Confined inside CNTs

Once the numbers of water molecules, $N_W$, have been determined from filling simulations as described above, see also Sec. III A, numerous simulations are performed to study the structure and dynamics of water encapsulated inside 10.07 nm armchair CNTs $(n, n)$ within the $NVT$ ensemble, where periodic boundary conditions are applied only along the CNT axis. All other parameters like force field, thermostat parameters, cut–off parameters, etc., are the same as in the filling simulations described in Sec. II B but without the use of a barostat. The water–water interaction is modeled in terms of the five–particle model TIP5P only [63].

When using conventional MD simulation techniques there are problems connected with the rare events of transitions between metastable structures of water inside CNTs, see our discussion in Sec. III C. This situation is illustrated here for the dimensionless net polarization of the water molecules along the CNT axis, $\mu$, which is defined as the average axial dipole moment divided by the number of molecules, $N_W$, and by the dipole moment of a single water molecule ($7.64 \times 10^{-30}$ Cm for the TIP5P model [63]). Hence, values of 1 and 0 indicate FE water and AF water, respectively, with FI water in between these limits.

As an example, we consider the time evolution of $\mu(t)$ for 177 water molecules inside CNT (8,8) shown in Fig. 1; similar examples can also be found in Refs. [43, 45]. For a temperature of 300 K there are only two conformational transitions connecting the three metastable states within the simulation time of 200 ns. (For 175 water molecules, the dynamics is even slower, see also our remarks in the beginning of Sec. III A). Obviously, the underlying timescales are so long because the transitions between states with grossly different polarizations involve concerted rotations of many (or even all) water molecules which is an extremely rare event. Hence, an ergodic sampling of the system's phase space with conventional MD simulations is out of reach with today's computational resources.

As an extension of conventional (single temperature NVT) MD, replica exchange MD (REMD) is based on an ensemble of non–interacting replica, i. e., independent simulations

for different temperatures. The REMD algorithm builds on the idea of a random walk in temperature space, where the exchange between neighboring replicas $i$ and $j$ is controlled by an extension of the Metropolis-Hasting expression for the acceptance probability [69]

$$P_{ij} = \min\{1, \exp[(\beta_i - \beta_j)(V(r_i) - V(r_j)]\} \tag{3}$$

which satisfies the detailed balance condition [50]. Here $\beta = \frac{1}{k_B T}$ is the inverse of temperature $T$ and $k_B$ is the Boltzmann constant. The potential energies $V$ are evaluated for $r$ specifying the positions of the particles in the replica systems. The REMD technique has the significant advantage, that the simulated systems can overcome barriers between local minima of the energy through exchanging configurations between two neighboring temperatures [48–50]. Hence, it is expected that REMD simulations sample the phase space more efficiently if the algorithm swaps, at sufficient frequency, forth and back between lower temperatures where the dynamics is impeded by relatively high barriers and higher temperatures where a broad sampling can be obtained more easily. To the best of our knowledge, REMD techniques are applied here for the first time to simulate water in CNTs where the transitions between various metastable FE, AF, FI water orientations are rare events because they involve concerted rotations of many water molecules.

The REMD simulations are performed using MPI GROMACS 4.5 [59]. The temperatures are distributed exponentially according to

$$T_n = T_0 e^{kn}, \quad 0 \leq n \leq N_T \tag{4}$$

where the temperatures range between $T_{min} = T_0$ and $T_{max} = T_0 e^{kN_T}$ and where the parameters $k$ and $N_T$ can be tuned to obtain temperature intervals allowing for sufficient acceptance probabilities which should be typically within $0.2 \ldots 0.3$ [59]. In some cases, however, it proved necessary to manually adjust the temperatures to meet this requirement. For a list of the temperatures actually used in our simulations, see Tab. I, where the distributions are ranging from $T_{min} = 200$ K, where all the water structures are frozen, to $T_{max} = 600$ K, where replicas are not trapped in local energy minima anymore. The number of temperatures, $N_T$, varies between 8 and 34, where $N_T$ increases with the CNT radius, to account for the increasing number of metastable structures, see our discussion in Sec. III B.

In practice, the REMD scheme is initialized by running conventional MD simulations of 1 ns length, to achieve equilibration for each of the temperatures separately. Then short

REMD simulations (100 ps) were carried out to validate the acceptance probability between adjacent replicas and/or to calibrate the above parameters $k$ and $N_T$ where exchanges are attempted every 1 ps. Afterwards, long REMD simulations (20 ns) are performed which are the basis of our analyis given in Sec. III C.

## III. RESULTS AND DISCUSSION

### A. Determination of CNT Water Filling

As a prerequisite for the investigations of water structure and dynamics in Secs. III B and III C, respectively, we first have to determine the water occupancy of CNTs, i. e. the number $N_W$ of water molecules entering spontaneously an open-ended CNT when immersed in water with a given temperature and pressure. Such filling simulations have occasionally been reported in the literature [25, 34, 70], however, without uniform results. In particular, a systematic investigation of the effects of different water–water and water–carbon force fields is still lacking; for a noteworthy exception, see [70].

In our investigation, MD simulations using the $NPT$ approach of Sec. III A are used to determine the number of water molecules, $N_W$, contained per unit length (1 nm) in different low–diameter CNTs for $T = 300$ K and $P = 10^5$ Pa. In order to study the influence of the force field on the spontaneous filling of various CNTs immersed in water, three series of simulations are performed. Here, due to the considerable effort of these simulations, relatively short armchair CNTs with $L = 1.47$ nm were chosen. While this short CNT length results in uncertainties shown as errorbars in Fig. 2, we emphasize that for the final determination of the water occupancy numbers much longer CNT fragments with $L \approx 10$ nm have been studied, see below.

First, the effect of employing different water–water interaction models on the water occupancy, $N_W$, is investigated for the case of CNT (8,8). Our results for isotropic water–carbon interaction, $\delta = 0$, are shown in panel (a) of Fig. 2. There, by varying the interaction strength $\eta$ between 0.25 kJ/mol and 1.5 kJ/mol, we simulate the hypothetical transition from a hydrophobic to hydrophilic nanotube. For all water models, our results essentially coincide with those obtained in Ref. [70] for the TIP3P water model: Below a certain threshold value which is nearly the same for the five water models and which is near $\eta = 0.33$

kJ/mol, water is repelled from the interior of the CNT. Above that value, the water filling quickly rises and reaches saturation earlier (e. g. at $\eta = 0.7$ kJ/mol for TIP5P) or later (e. g. at $\eta = 1.4$ kJ/mol for TIP3P). Interestingly, the discrepancies in the intermediate regime may be assigned to qualitatively different water structures. For example, as was already noted in Ref. [43], water inside CNT (8,8) forms tetragonal or pentagonal ice nanotubes in simulations with TIP4P or TIP5P, respectively.

Second, the effect of the anisotropy $\delta$ of the water–carbon interaction on the water occupancy, $N_W$, is investigated here for CNTs of different diameter. In contrast to the interaction strength $\eta$, the anisotropy $\delta$ practically does not affect $N_W$ as shown in Fig. 2 (b). Only for CNT (10,10) there is a weak minimum around $\delta = 1.5$. Note, however, that the water structure does depend on $\delta$, in some cases even qualitatively, see our previous work [47].

Finally, the effect of interaction strength $\eta$ on the water occupancy, $N_W$, inside CNTs of different diameters is shown in panel (c) of Fig. 2. The threshold for interior wetting of CNTs is highest for the smallest CNT(5,5) investigated here ($\eta \approx 0.5$ kJ/mol). The lowest threshold values, between 0.25 and 0.325 kJ/mol, are found for CNT (8,8) and (9,9) which is in qualitative agreement with previous work [70]. Finally, for water inside CNT (10,10) the threshold is higher again, displaying an almost stepwise increase at $\eta = 0.425$ kJ/mol. Also the saturation value is found to depend sensitively on the CNT diameter: For example, in CNT(6,6) saturation is already reached for interaction strengths $\eta > 0.425$ kJ/mol, in other cases the water occupancy continues to rise with increasing $\eta$ up to (at least) 1.5 kJ/mol which is most pronounced for CNT (7,7) and CNT (10,10), indicating a higher compressibility of water inside these structures.

In summary, the above test calculations show that the water occupancy reached by spontaneous filling of CNTs immersed in water at ambient conditions depends only very weakly on the choice of the water model. Hence, in the following we choose the TIP5P model because – at least for bulk water – it is known to be superior to the other models; in particular, it reproduces the density anomaly and the melting point [63]. Moreover, the filling behavior of CNTs does practically not depend on the anisotropy parameter, $\delta$, of the water–carbon LJ interaction model, either, and only weakly on its overall interaction strength $\eta$, provided this value exceeds the threshold value. Consequently, in the remainder of this work we will use the values $\eta = 1$ kJ/mol and $\delta = 1$ for the carbon–water interaction, as suggested in our previous work [47] and also in other work on water outside CNTs [57].

With this choice of force field parameters, our main simulations of water filling are conducted for 30 different CNTs of considerable length ($L \approx 10$ nm, see Sec. III A), with diameters $d$ between 0.54 nm and 2.8 nm, both zigzag $(n, 0)$ with $8 \leq n \leq 20$ and armchair $(n, n)$ nanotubes with $4 \leq n \leq 20$. Their diameters are related to the helicity indices $(n, m)$ through

$$d = \frac{\sqrt{3}a}{\pi}\sqrt{n^2 + nm + m^2} \tag{5}$$

In our simulations the CNTs are solvated in $14 \times 14 \times 20$ nm$^3$ periodic water boxes. Our results for the dependence of the number of water molecules, $N_W$, on the CNT diameter are given in Tab. II. They are obtained as time averages over 10 ns (including an equilibration of 1 ns) where the outer $2 \times 5$ ($2 \times 3$) unit cells or $2 \times 1.23$ nm ($2 \times 1.28$ nm) for armchair (zigzag) CNTs are not considered, in order to avoid edge effects. We note that (5,5) is the smallest armchair CNT to fill with water spontaneously at ambient conditions, and (9,0) is the smallest zigzag CNT.

The corresponding densities can be obtained from $\rho = M/V$, where $M$ is the total mass of the confined water molecules and where $V$ is the available volume inside a CNT of length $L$

$$V = \frac{\pi}{4}L(d - d_C)^2 \tag{6}$$

where $d_C = 0.34$ nm is the van der Waals diameter of carbon [58]. For the smaller CNTs, the water density $\rho$ is found to be strongly undulated, see Fig. 3. There are two pronounced maxima reaching up to $\rho \approx 1.2$ g/cm$^3$ at $d = 0.68$ and $d = 1.08$ nm, corresponding to CNT (5,5) and CNT (8,8). Two minima are found at $d = 0.86$ nm and $d = 1.41$ nm, corresponding to CNT (11,0) and CNT (18,0). Finally, with the diameter increasing beyond $\approx 1.6$ nm, the water density converges smoothly toward the bulk value of 1 g/cm$^3$.

### B. Ice Nanotube Structures and Net Polarizations

This section is concerned with structure, energetics, and polarization of water confined inside selected armchair CNTs $(n, n)$ of length $L = 10.07$ nm, with periodic boundary conditions along the CNT axis. We will discuss minimum energy structures which are obtained by means of a steepest decent algorithm implemented in the GROMACS 4.5 software package [59]. In order to sample the plethora of local minima of the high–dimensional potential energy landscapes, a large number of energy minimizations were performed, which were

initialized from snapshots of REMD trajectories (see Sec. II C). In many cases these minimizations resulted in INT structure consisting of several domains. Except where noted below, however, we discuss here only structures found for domains extending over lengths of at least 1 nm.

In the calculations of INT structures discussed here the number of water molecules, $N_W$, is taken from the results of the filling simulations of open-ended CNTs discussed above. By appropriate scaling of the water occupancy (per unit length of 1 nm) summarized in Tab. II, we obtain $N_W = 36, 39, 104, 173, 210, 278$ for CNT $(n, n)$, $5 \leq n \leq 10$. With the exception of water inside CNTs (5,5) and (6,6), all minimum energy structures are found to be single-walled ice nanotube (INT) structures which are compatible with the Bernal–Fowler rules for tetrahedral hydrogen bonding [1, 37]. In particular, trigonal, pentagonal, hexagonal and octagonal INTs were found for CNT (7,7), (8,8), (9,9) and (10,10), respectively. However, to avoid excessive defects leading to reduced stabilty, we had to ensure that the numbers $N_W$ are integer multiples of 3, 5, 6, and 8. Hence, we chose $N_W = 102, 175, 210, 280$ for simulations of water inside CNT $(n, n)$, $7 \leq n \leq 10$, throughout the remainder of this work.

Top views of selected structures are shown in Fig. 4; a complete overview of all INT structures can be found in Tab. III and in Fig. 5 where the unrolled representations conveniently reveal the network of the hydrogen bonds. In analogy to the indices $(m, n)$ for CNT structures, also the single–walled INTs are denoted here by chiral indices $\langle \tilde{m}, \tilde{n} \rangle$ in angle brackets, where $\tilde{n} = 0, 1, 2$ stand for prisms, single, and double helices, respectively [33].

### 1. *Water chains inside CNT (5,5) and CNT (6,6)*

Water inside CNTs (5,5) and (6,6) forms quasi one-dimensional water chains as shown in Fig. 5 A and A*, respectively. The arrangement of oxygen atoms in water structure A is nearly linear because the CNT (5,5) has a very small interior diameter, $d - d_C = 0.34$ nm. Since the CNT (6,6) has a slightly larger diameter, $d - d_C = 0.48$ nm, the arrangement of oxygen in structure A* is in a zigzag pattern, thus allowing for a closer to linear geometry of the H-bonds. As shown in Tab. III, the polarizations $\mu$ of water inside CNT (5,5) and (6,6) are rather high in both cases, but nearly ten percent higher for CNT (5,5) because of the lower tilt angle between the molecular dipoles and the CNT axis. Consequently, in

agreement with previous results, these water chains are strongly FE [28].

The corresponding values of the water–water interaction energy $E_{\mathrm{W-W}}$ are also given in Tab. III. For water inside CNT (6,6) this energy is notable stronger than for water inside CNT (5,5) because of the more favorable geometry for H–bonding. Conversely, the water–carbon attraction $E_{\mathrm{W-C}}$ is higher for CNT (5,5) than for CNT (6,6), because the smaller diameter of the former leads to water interacting with more carbon atoms.

### *2. Trigonal INTs inside CNT (7,7)*

The only minimum energy structure found for water inside CNTs (7,7) is the $\langle 3,1\rangle$ single helix INT structure B, see Figs. 4 and 5. Its polarization $\mu$ is among the highest values in Tab. III, thus rendering this structure highly FE. Because every water molecule is involved in four hydrogen bonds, the energy $E_{\mathrm{W-W}}$ is much stronger than for water inside CNT (5,5) and (6,6) whereas $E_{\mathrm{W-C}}$ is much weaker due to the larger CNT diameter.

### *3. Pentagonal INTs inside CNT (8,8)*

The minimum energy structures for water inside CNT (8,8) can be assigned to three different classes of pentagonal INTs, i. e. $\langle 5,0\rangle$ prisms (C, D, E), as well as $\langle 5,1\rangle$ single helix (F) and $\langle 5,2\rangle$ double helix (G), see Figs. 4, 5, and Tab. III. Note that pentagonal prisms were already proposed in Refs. [33, 41] while the single helix was found in Ref. [43]. Also the double helix structure was predicted in the literature recently, but only in the presence of external electric fields [46]. In addition to these structures of the network of the O–atoms, especially the proton ordering is of interest which is given by the notation u:d (indicating the ratio of water dipoles pointing up and down) in the central columns of Tab. III. For the $\langle 5,0\rangle$ prism we find a 5:0 FE water structure (E) with all water dipoles pointing toward the same direction and also 4:1 and 3:2 FI water structures (D and C) where the proton ordering is reversed in one or two of the five water strands along prism edges, respectively. In contrast, for the $\langle 5,1\rangle$ single helix (F) and for the $\langle 5,2\rangle$ double helix (G) only 5:0 FE proton ordering is found. Apparently, dictated by the proton ordering and the tilt angle between dipole direction and the proton orientation, the ordering of INT phases according to their polarizations $\mu$ is $G > F > E > D > C$, see also Tab. III. While the water–carbon

interaction energy $E_{\mathrm{W-C}}$ is very similar for all pentagonal INT structures inside CNT (8,8), the single helix (F) has the lowest water–water interaction energy $E_{\mathrm{W-W}}$ of the five (also compared with all structures inside different CNTs presented below). Hence, we cannot confirm the statement of Ref. [41], claiming that the FI $\langle 5,0\rangle$ INT structure C with 3:2 proton ordering would be most stable, due to the dipole–dipole interaction.

*4. Hexagonal INTs inside CNT (9,9)*

For water inside CNT (9,9), we found two classes of hexagonal INT structures, i. e., the $\langle 6,0\rangle$ prisms (H–K) and the $\langle 6,1\rangle$ single helix (L), again in accordance with previous work published in Ref. [33, 41, 42] and [43], respectively. In close analogy to the case of CNT (8,8), in the $\langle 6,1\rangle$ single helix (L) the molecules prefer a FE (6:0) arrangement, while for the prisms there exist both 6:0 FE (K) and 5:1 FI (J) structures with the proton ordering in one water strand being reversed. Furthermore, several 4:2 FI (I) and also 3:3 AF (H) water arrangements are found; however those structures extend only over shorter domains of the nanotubes, as indicated by the colored boxes in Fig. 5. The resulting polarizations $\mu$ are ordered as $L > K > J > I > H$, while the energies $E_{\mathrm{W-W}}$ and $E_{\mathrm{W-C}}$ are identical for structures J, K, and L.

*5. Octagonal INTs inside CNT (10,10)*

For water inside CNT (10,10), we find exclusively octagonal INT structures in our simulations based on the TIP5P water model (whereas for TIP3P heptagonal INTs are found [42]). In our simulation we encounter two classes of INT structures, i. e., the $\langle 8,0\rangle$ prisms (M–Q) and the $\langle 8,1\rangle$ single helix (R). While for the helix the FE (8:0) proton–ordered arrangement is the only one, various schemes can occur for the prism: In addition to the FE (8:0) structure, several other patterns are found. These are the 7:1 (P), 6:2 (O), 5:3 (N) FI structures as well as the 4:4 AF structure M which differ from each other in the arrangement of the different water strands (along prism edges) with up and down orientation. The different INT structures inside CNT (10,10) can be ordered according to their polarizations $\mu$ as $R > Q > P > O > N > M$ where again the energies $E_{\mathrm{W-W}}$ and $E_{\mathrm{W-C}}$ are nearly degenerate.

### C. Temperature Effects and Structural Transitions

In this section we are dealing with thermal effects and structural transitions of water confined inside CNTs $(n, n)$, $5 \leq n \leq 10$. In particular, we address the question which of the various INT structures introduced above appear at which temperature with which relative population. Furthermore it will be of interest, at which temperatures structural transitions occur and whether the observables of interest change continuously or not, and whether latent heats can be assigned. All of the investigations disscussed here are based on REMD simulations within the $NVT$ setting; for technical details see Sec. II C.

Because the main focus of our work is on the question of proton ordering inside CNTs, leading to FE, FI, and AF proton–ordered arrangements, these questions will be, foremost, discussed here in terms of probability distributions of the dimensionless polarization $\mu$ introduced in Sec. II C, for representative temperatures from our REMD simulations, see Fig. 6. Note that if we assume the probability of the orientation of $\mu$ to be equally distributed over a sphere, then the probability of finding an angle $\theta$ between the water polarisation and the CNT axis would be $f(\theta) \propto \cos\theta$, reflecting the surface element in spherical coordinates. Hence, with $\mu \equiv \sin\theta$ we obtain the following relation

$$f(\mu) \propto \cos(\arcsin\mu) = \sqrt{1-\mu^2} \tag{7}$$

giving the probability of finding a value $\mu$ under the above assumption of equally distributed water orientations. For additional investigations of the temperature dependence of the polarization, we define certain polarization states by assigning intervals of $\mu$, guided by the values listed in Tab. III, and we show their relative populations in the temperature range from 200 K to 600 K in Fig. 7.

To further characterize structural transitions, we also consider the decomposition of the averaged energies into kinetic energy, LJ (water–carbon and water–water) and Coulomb (water–water only) potential energies, see Fig. 8. Note that the water–water potential energy is also used to determine the latent heat for INT structural transitions. In agreement with the equipartition principle, our values for the kinetic energy practically coincide with $N_D k_B T/2$ where the number of degrees of freedom is $N_D = 6N_W$ for water with frozen bond lengths and bond angle.

As yet another way to analyze the structure of water in CNTs, we also analyse the H-bonding networks obtained from our REMD simulations as shown in Fig. 9. While already

the average number of hydrogen–bonds can provide valuable insight for water in small CNTs [31, 71], more detailed information is provided by the joint probabilities $p(n_a, n_d)$ of a water molecule to act $n_a$ times as an acceptor and $n_d$ times as a donor in hydrogen bonding [72]. To account for the floppy arrangement of water molecules in our simulations, we use a relaxed criterion for the detection of H-bonds, i. e. , O–O distance up to 0.35 nm and deviation from linearity of the O–H $\cdots$ O arrangement up to 45 degrees.

### 1. *Water chains inside CNT (5,5) and CNT (6,6)*

For $T = 200$ K the histograms of the polarizations $\mu$ for water confined in CNT (5,5) and CNT (6,6) display narrow single peak distributions, see Fig. 6. The high $\mu$ values correspond to those of FE structures A and A* in Fig. 5 and Tab. III. Even when increasing the temperature up to 600 K, these distributions are essentially not changing, so there are no structural transitions, i. e., for the most part the water molecules remain connected in chain–like structures A and A*, due to the confinement effect inside the very narrow CNTs. However, due to angular fluctuations, the polarizations $\mu$ slightly decrease with increasing temperature while the distributions become wider.

The absence of structural transitions is further corroborated by the energies shown in Fig. 8; none of the curves for CNT (5,5) or (6,6) shows a significant inflection. The corresponding H–bonding probabilities for CNT (5,5) and (6,6) are shown in the leftmost two columns of Fig. 9. The leading probability $p(1,1)$ is indicative of a quasi–linear chain. For water structure A inside CNT (5,5), this probability remains low ($< 0.5$), which is a consequence of the non-linear arrangement of the O–H$\cdots$O hydrogen-bonds inside the narrow CNT interior, see also our discussion in Sec. III B. For increasing temperature, the O–atoms start to deviate from linearity, thus yielding a slight rise in $p(1,1)$. For water structure A* inside CNT (6,6), this probability decreases from near unity at $T = 200$ K to about 0.6 at $T = 600$ K while the probabilities $p(1,0) \approx p(0,1)$ increase conversely. Obviously, this is due to the enhanced fluctuations leading to (temporally and spatially limited) chain ruptures.

*2. Trigonal INTs inside CNT (7,7)*

For $T = 200$ K the histogram of polarization $\mu$ for water confined in CNT (7,7) displays a narrow peak corresponding to the FE INT $\langle 3, 1\rangle$ helix structure B, see also Figs. 4, 5 and Tab. III. For $T = 326$ K and $T = 368$ K, the distributions become slightly broader but they are still centered at rather high values of 0.85 and 0.83, respectively, which indicates that helical the FE $\langle 3, 1\rangle$ INT structure is essentially intact. For $T = 600$ K, however, the polarization exhibits a wide distribution peaking at $\mu = 0$ indicating a substantial loss of ordering. The fact that this distribution is considerably narrower than predicted from Eq. (7), however, suggests that the loss of proton ordering is not complete. The remaining preference of the water plane being perpendicular to the CNT direction may be caused by the minima of the water–CNT potentials for either O or H atoms pointing toward the nanotube wall. Note that there is also a "shoulder" at $\mu \approx 0.6$ which is due to configurations where the $\langle 3, 1\rangle$ INT structure is still found, but only for short spatial domains, interspersed by numerous defects.

To investigate the temperature dependence of water structures inside CNT (7,7) in more detail, we define three different polarization states. Values of $0.88 \leq \mu \leq 1$ represents (almost) intact $\langle 3, 1\rangle$ helical FE INT structure B. Between $T = 250$ K and $T = 400$ K the population of this state decays from 1 to 0, see Fig. 7. At intermediate temperatures, most population is found for $0.85 \leq \mu < 0.88$ which describes INT structures with partial proton disordering. Finally, a state with $0 \leq \mu < 0.85$ representing irregular INT structures takes over for $T \geq 400$ K. It is emphasized that this structural transition occurs very smoothly. This is also confirmed by the energy decomposition shown in Fig. 8 where all curves for water in CNT (7,7) show only a very weak inflection around 250 - 400 K. Hence, neither a clear transition temperature nor a latent heat can be defined. The gradual disruption of the H–bonding networks is also shown in Fig. 9. Between $T = 250$ K and $T = 400$ K the joint probability $p(2, 2)$ indicating tetrahedric H-bonding in INTs decreases drastically, while there are increasing probabilities of defects (two–, three-, and even five-fold coordinations) which are known to catalyse the diffusion and reorientation of water molecules [72].

### 3. *Pentagonal INTs inside CNT (8,8)*

The single peak in the $T = 200$ K distribution (Fig. 6) for water confined inside CNT (8,8) corresponds to the $\langle 5,1\rangle$ single helix INT structure F which is highly FE and which is lowest in energy, see Tab. III. At $T = 470$ K there is an additional peak at even higher $\mu$ indicating the existence of the FE $\langle 5,2\rangle$ double helix INT structure G. For increasing temperature ($T = 515$ K) these INT structures become more and more disordered, and the two peaks become wider and start to overlap. At even higher temperature ($T = 600$ K), the polarization distribution is again qualitatively similar to Eq. (7), thus indicating a substantial loss of proton ordering. Note that clear signatures of the FI structures C, D or the FE structure E shown in Fig. 5 could not be detected for any of the temperatures in our REMD ensemble.

The temperature dependence of the corresponding populations is shown in Fig. 7. While only the single helical state F is populated for temperatures up to 400 K, for the highest temperatures ($\geq 600$ K), no clear assignments can be made anymore. The double helical state G, which is found at intermediate temperatures around 470 K, can be regarded as a transition state. From the energy representation in Fig. 8, we see a slightly stronger inflection of the curves than for water inside the smaller CNTs discussed above, but the transition is still relatively smooth. This is also supported by Fig. 9 showing a monotonous fall of the tetrahedric H–bonding probability $p(2,2)$ with increasing temperature, along with an increase of the probabilities of various defects.

### 4. *Hexagonal INTs inside CNT (9,9)*

For water confined inside CNT (9,9), the distribution of polarization $\mu$ shows already for our lowest temperature (200 K) two separate peaks, see Fig. 6. They are readily assigned to the FE $\langle 6,0\rangle$ hexagonal prism structure K and the FE $\langle 6,1\rangle$ single helix structure L, respectively, which happen to be isoenergetic for the force fields used here, see Tab. III. Already for slightly higher temperature (218 K), the signature of structure L nearly disappears and there is a new small peak due to the FI $\langle 6,0\rangle$ prism J with 5:1 proton ordering. When increasing the temperature from 362 K (not shown) to 370 K, the distribution suddenly becomes very wide. However, the INT structure is not yet completely irregular as can be

seen from the four plateaus of the distributions, which are reminiscent of AF structure H, FI structures I and J, and FE structure K, all of which are different $\langle 6,0\rangle$ prisms, but with different proton ordering schemes 3:3, 4:2, 5:1, and 6:0, respectively. However, as mentioned already in Sec. III B, these structures are only found for shorter domains, with many fluctuations and defects.

The two structural transitions of water confined in CNT (9,9) can be clearly seen in Figs. 7, 8 and 9. At 218 K there is a sudden structural transition from the $\langle 6,1\rangle$ helical structure L to the $\langle 6,0\rangle$ prism structure K. At 362 K the INT structure gets strongly perturbed with many defects occuring, and the fluctuations increase suddenly. Consequently, this transition is termed melting–like here which is also supported by Fig. 8 displaying an almost stepwise increase of the water potential energy at 362 K. This resembles a first–order transition, in accordance with the conclusions in Ref. [33]. The corresponding latent heat of 8.0 kJ/mol is obtained from linear fits to the water–water potential energy below and above the transition temperature.

#### *5. Octagonal INTs inside CNT (10,10)*

For water confined inside CNT (10,10), almost all of the minimum energy octagonal INT structures discussed in Sec. III B appear already at 200 K, see Fig. 6. The FE helix $\langle 8,1\rangle$ structure R coexists with various prism $\langle 8,0\rangle$ structures, in particular AF structure M and FI structures N, O, P, which differ from each other with respect to the proton ordering schemes, see also Tab. III. Up to a temperature of 285 K, the populations of the respective polarization states shown in Fig. 7 do not follow any conclusive trend. Beyond that temperature, the confined water abruptly looses its INT structure, favouring low values of polarization $\mu$. As is also confirmed by the near–discontinuities of the curves for water inside CNT (9,9) in Figs. 8 and 9, this melting–like transition again resembles a first–order phase transition, and we estimate a latent heat of 4.4 kJ/mol.

## IV. CONCLUSION

In the first series of simulations, we investigated the water occupancy of open–ended armchair and zigzag CNTs immersed in water, with diameters from 0.54 nm and 2.7 nm and

with a length of $\approx 10$ nm. Using MD simulations of CNTs under ambient $NPT$ conditions, the number of water molecules spontaneously filling the CNTs was determined for different interaction models. Comparing simulations with SPC, SPCE, TIP3P, TIP4P, and TIP5P water models, we found that the details of the water–water interaction have only a minor influence. Moreover, the anisotropy parameter $\delta$ of the water–carbon interaction doesn't have much influence either. However, when varying the total water–carbon interaction strength $\eta$, there is a clear threshold separating a hydrophobic regime, where water does not enter the CNTs, and a hydrophilic regime, where water molecules spontaneously enter the CNTs until a saturation density is reached. For the subsequent simulations, the value $\eta = 1$ kJ/mol was used which is well in the latter regime. In contrast to most of the simulations published previously where empirical LJ parameters were used, this value was taken from our previous parametrization [47] of high–level CCSD(T) quantum chemistry results for the water–graphene interaction [53] which also support a substantial anisotropy, $\delta = 1$. In ongoing work this procedure will be repeated for CNTs of different diameters, in order to directly assess the effect of curvature on the water adsorption energy [73].

Based on the results of these filling simulations, we investigated water structures encapsulated in armchair CNTs $(n, n)$, $5 \leq n \leq 10$, under $NVT$ conditions for CNTs of $\approx 10$ nm length with periodic boundaries. Inside the smallest nanotubes ($n = 5, 6$) we found highly FE, quasi–one–dimensional water chains. For the other CNTs ($n \geq 7$) water molecules arrange into single–walled INTs where the binding energy per water molecule decreases notably from $n = 7$ to $n = 8$, beyond which it slowly rises again. This is in line with results for water clusters encapsulated in CNTs, where a minumum of this energy was observed near $d = 1$ nm [74].

For every armchair CNT with $n \geq 8$, we found several different minimum energy INT structures which are – in most cases – close to isoenergetic, in spite of the different helicity of the networks formed by the O–atoms: Single helical structures were found for $7 \leq n \leq 10$, in all cases only in FE arrangement, with all water molecules oriented the same way. In addition, a double helical INT structure was found for $n = 8$ which is FE with a polarization even exceeding that of any of the single helices. Prism–like structures were found only for $8 \leq n \leq 10$ with various FE, FI, and AF (only for $n = 9, 10$) orientation schemes. Out of all the FE structures which we compiled in Tab. III, the sequence of polarization strengths is as follow: $A > G > B > A* > F > L > R > Q > K$.

The coexistence of minimum energy structures with very similar energies but very different proton ordering (and hence, very different polarizations) presents a major challenge to finite temperature simulations of structure and dynamics of the confined INTs. The various FE, FI, and AF water structures mentioned above are highly metastable, with high barriers that cannot be overcome by conventional MD simulations for e. g. $T = 300$ K. Hence, we had to resort to REMD simulation techniques to obtain the populations of the different INT states. Their temperature dependence revealed that, despite of thermal fluctuations, many of the FE INT structures confined in low–diameter CNTs are stable at room temperature, as already claimed, e. g., in Ref. [43]. In addition, several transition phenomena were found: First, we found helix–helix and helix–prism structural transitions which can be either continuous (around 470 K for $n = 8$) or discontinuous (at 218 K for $n = 9$). Second, melting–like (solid–liquid) transitions were detected in which the INT structures are disrupted leading to a loss FE, FI, or AF proton ordering. Also these transitions can be either smooth (for $n = 7, 8$) or abrupt, first–order transitions in which case it was possible to extract transition temperatures of $T = 362$ K for $n = 9$ and $T = 285$ K for $n = 10$, the latter of which is already close to the bulk melting temperature. These findings are in line with the study of ambient pressure [33] and high-pressure [38] water inside CNTs where it was also found that hexagonal and heptagonal INTs exhibit first-order freezing transitions while for smaller INTs the transitions are smooth. We note that the transition temperatures found in Refs. [33, 38, 41] are much lower. This may be due to the use of other water–carbon force fields and, most likely, due to the use of the TIP4P potential which is known to predict a too low melting temperature for bulk water [75, 76].

Finally, another interesting feature can be seen in Fig. 9 showing an asymmetry between donor and acceptor H-bonding probabilities, $p(1,2) < p(2,1)$ and $p(2,3) > p(3,2)$, for INTs inside CNTs (7,7) and (8,8). This is also found for INTs confined in CNTs (9,9) and (10,10) but only below the respective melting temperatures of 362 K and 285 K. Beyond these temperatures, these asymmetries are reversed, as is also the case for bulk water where, e. g., the probability for triply coordinated water molecules to accept two hydrogen bonds is lower than that to donate two hydrogen bonds, i. e., $p(1,2) > p(2,1)$ [72].

**ACKNOWLEDGMENTS**

S. L. is grateful to the Chinese Scholarship Council for financial support. Helpful discussions with Kurt Liebers and Dr. Shulai Lei are acknowledged.

[1] J. D. Bernal and R. H. Fowler, J. Chem. Phys. **1**, 515 (1933).

[2] S. T. Bramwell, Nature **397**, 212 (1999).

[3] T. Bartels-Rausch, V. Bergeron, J. H. E. Cartwright, R. Escribano, J. L. Finney, H. Grothe, P. J. Gutiérrez, J. Haapala, W. F. Kuhs, J. B. C. Pettersson, S. D. Price, C. I. Sainz-Díaz, D. J. Stokes, G. Strazzulla, E. S. Thomson, H. Trinks, and N. Uras-Aytemiz, Rev. Mod. Phys. **84**, 885 (2012).

[4] P. Parkkinen, S. Riikonen, and L. Halonen, J. Phys. Chem. C **118**, 26264 (2014).

[5] L. Pauling, J. Am. Chem. Soc. **57**, 2680 (1935).

[6] W. F. Giauque and J. W. Stout, J. Am. Chem. Soc. **58**, 1144 (1936).

[7] E. O. Wollan, W. L. Davidson, and C. G. Shull, Phys. Rev. **75**, 1348 (1949).

[8] J. C. Li, V. M. Nield, D. K. Ross, R. W. Whitworth, C. C. Wilson, and D. A. Keen, Philos. Mag. Part B **69**, 1173 (1994).

[9] G. P. Johari and S. J. Jones, J. Chem. Phys. **62**, 4213 (1975).

[10] H. Wang, R. C. Bell, M. J. Iedema, A. A. Tsekouras, and J. P. Cowin, Astrophys. J. **620**, 1027 (2005).

[11] H. Fukazawa, A. Hoshikawa, Y. Ishii, B. C. Chakoumakos, and J. A. Fernandez-Baca, Astrophys. J. **652**, L57 (2006).

[12] S. M. Jackson, V. M. Nield, R. W. Whitworth, M. Oguro, and C. C. Wilson, J. Phys. Chem. B **101**, 6142 (1997).

[13] Y. Tajima, T. Matsuo, and H. Suga, J. Phys. Chem. Sol. **45**, 1135 (1984).

[14] T. Matsuo, Y. Tajima, and H. Suga, J. Phys. Chem. Sol. **47**, 165 (1986).

[15] H. Fukazawa, A. Hoshikawa, H. Yamauchi, Y. Yamaguchi, and Y. Ishii, J. Cryst. Growth **282**, 251 (2005).

[16] M. Arakawa, H. Kagi, and H. Fukazawa, J. Mol. Struct. **972**, 111 (2010).

[17] C. G. Salzmann, P. G. Radaelli, A. Hallbrucker, E. Mayer, and J. L. Finney, Science **311**,

1758 (2006).

[18] C. G. Salzmann, P. G. Radaelli, E. Mayer, and J. Finney, Phys. Rev. Lett. **103**, 105701 (2009).

[19] I. M. Svishchev and P. G. Kusalik, Phys. Rev. Lett. **73**, 975 (1994).

[20] X. Su, L. Lianos, Y. Shen, and G. Somorjai, Phys. Rev. Lett. **80**, 1533 (1998).

[21] M. J. Iedema, M. J. Dresser, D. L. Doering, J. B. Rowland, W. P. Hess, A. A. Tsekouras, and J. P. Cowin, J. Phys. Chem. B **102**, 9203 (1998).

[22] D. N. LeBard and D. V. Matyushov, J. Phys. Chem. B **114**, 9246 (2010).

[23] H.-X. Zhao, X.-J. Kong, H. Li, Y.-C. Jin, L.-S. Long, X. C. Zeng, R.-B. Huang, and L.-S. Zheng, Proc. Natl. Acad. Sci. **108**, 3481 (2011).

[24] T. Croteau, A. K. Bertram, and G. N. Patey, J. Phys. Chem. A **114**, 8396 (2010).

[25] G. Hummer, J. C. Rasaiah, and J. P. Noworyta, Nature **414**, 188 (2001).

[26] A. Berezhkovskii and G. Hummer, Phys. Rev. Lett. **89**, 064503 (2002).

[27] C. Dellago, M. Naor, and G. Hummer, Phys. Rev. Lett. **90**, 105902 (2003).

[28] J. Köfinger, G. Hummer, and C. Dellago, Proc. Natl. Acad. Sci. **105**, 13218 (2008).

[29] L. Wang, J. Zhao, F. Li, H. Fang, and J. P. Lu, J. Phys. Chem. C **113**, 5368 (2009).

[30] W. H. Noon, K. D. Ausman, R. E. Smalley, and J. Ma, Chem. Phys. Lett. **355**, 445 (2002).

[31] J. Wang, Y. Zhu, J. Zhou, and X.-H. Lu, Phys. Chem. Chem. Phys. **6**, 829 (2004).

[32] J. Bai, J. Wang, and X. C. Zeng, Proc. Natl. Acad. Sci. **103**, 19664 (2006).

[33] D. Takaiwa, I. Hatano, K. Koga, and H. Tanaka, Proc. Natl. Acad. Sci. **105**, 39 (2008).

[34] A. Alexiadis and S. Kassinos, Chem. Eng. Sci. **63**, 2047 (2008).

[35] R. J. Mashl, S. Joseph, N. R. Aluru, and E. Jakobsson, Nano Lett. **3**, 589 (2003).

[36] J. Bai, C.-R. Su, R. D. Parra, X. C. Zeng, H. Tanaka, K. Koga, and J.-M. Li, J. Chem. Phys. **118**, 3913 (2003).

[37] K. Koga, R. D. Parra, H. Tanaka, and X. C. Zeng, J. Chem. Phys. **113**, 5037 (2000).

[38] K. Koga, G. T. Gao, H. Tanaka, and X. C. Zeng, Nature **412**, 802 (2001).

[39] A. Kolesnikov, J.-M. Zanotti, C.-K. Loong, P. Thiyagarajan, A. Moravsky, R. Loutfy, and C. Burnham, Phys. Rev. Lett. **93**, 035503 (2004).

[40] Y. Maniwa, H. Kataura, M. Abe, A. Udaka, S. Suzuki, Y. Achiba, H. Kira, K. Matsuda, H. Kadowaki, and Y. Okabe, Chem. Phys. Lett. **401**, 534 (2005).

[41] C. Luo, W. Fa, J. Zhou, J. Dong, and X. C. Zeng, Nano letters **8**, 2607 (2008).

[42] F. Mikami, K. Matsuda, H. Kataura, and Y. Maniwa, ACS nano **3**, 1279 (2009).

[43] Y. Nakamura and T. Ohno, Phys. Chem. Chem. Phys. **13**, 1064 (2011).

[44] Y. Nakamura and T. Ohno, in *Molecular Dynamics - Studies of Synthetic and Biological Macromolecules*, edited by L. Wang (IOnTech, 2012) p. 297.

[45] Y. Nakamura and T. Ohno, Mat. Chem. Phys. **132**, 682 (2012).

[46] Y. He, G. Sun, K. Koga, and L. Xu, Sci. Rep. **4**, 6596 (2014).

[47] G. Pérez-Hernández and B. Schmidt, Phys. Chem. Chem. Phys. **15**, 4995 (2013).

[48] R. Swendsen and J. Wang, Phys. Rev. Lett. **57**, 2607 (1986).

[49] U. H. Hansmann, Chem. Phys. Lett. **281**, 140 (1997).

[50] Y. Sugita and Y. Okamoto, Chem. Phys. Lett. **314**, 141 (1999).

[51] Y. Okamoto, J. Mol. Graph. Mod. **22**, 425 (2004).

[52] S. Trebst, M. Troyer, and U. H. E. Hansmann, J. Chem. Phys. **124**, 174903 (2006).

[53] E. Voloshina, D. Usvyat, M. Schütz, Y. Dedkov, and B. Paulus, Phys. Chem. Chem. Phys. **13**, 12041 (2011).

[54] J. H. Walther, R. Jaffe, T. Halicioglu, and P. Koumoutsakos, J. Phys. Chem. B **105**, 9980 (2001).

[55] A. Alexiadis and S. Kassinos, Chem. Rev. **108**, 5014 (2008).

[56] T. Werder, J. H. Walther, R. L. Jaffe, T. Halicioglu, and P. Koumoutsakos, J. Phys. Chem. B **107**, 1345 (2003).

[57] M. Kaukonen, A. Gulans, P. Havu, and E. Kauppinen, J. Comp. Chem. **33**, 652 (2012).

[58] A. Bondi, J. Phys. Chem. **68**, 441 (1964).

[59] B. Hess, C. Kutzner, D. van der Spoel, and E. Lindahl, J. Chem. Theo. Comp. **4**, 435 (2008).

[60] H. J. C. Berendsen, J. P. M. Postma, W. F. van Gunsteren, and J. Hermans, in *Intermolecular Forces*, Vol. 14, edited by A. Pullman (Springer, 1981) pp. 331–342.

[61] H. J. C. Berendsen, J. R. Grigera, and T. P. Straatsma, J. Phys. Chem. **91**, 6269 (1987).

[62] W. L. Jorgensen, J. Chandrasekhar, J. D. Madura, R. W. Impey, and M. L. Klein, J. Chem. Phys. **79**, 926 (1983).

[63] M. W. Mahoney and W. L. Jorgensen, J. Chem. Phys. **112**, 8910 (2000).

[64] S. Miyamoto and P. A. Kollman, J. Comp. Chem. **13**, 952 (1992).

[65] G. Bussi, D. Donadio, and M. Parrinello, J. Chem. Phys. **126**, 014101 (2007).

[66] H. J. C. Berendsen, J. P. M. Postma, W. F. van Gunsteren, A. DiNola, and J. R. Haak, J.

Chem. Phys. **81**, 3684 (1984).

[67] T. Darden, D. York, and L. Pedersen, J. Chem. Phys. **98**, 10089 (1993).

[68] U. Essmann, L. Perera, M. L. Berkowitz, T. Darden, H. Lee, and L. G. Pedersen, J. Chem. Phys. **103**, 8577 (1995).

[69] N. Metropolis, A. W. Rosenbluth, M. N. Rosenbluth, A. H. Teller, and E. Teller, J. Chem. Phys. **21**, 1087 (1953).

[70] M. Melillo, F. Zhu, M. A. Snyder, and J. Mittal, J. Phys. Chem. Lett. **2**, 2978 (2011).

[71] M. Gordillo and J. Marti, Chem. Phys. Lett. **329**, 341 (2000).

[72] N. Agmon, Acc. Chem. Res. **45**, 63 (2012).

[73] S. Lei, S. Li, B. Paulus, and B. Schmidt, to be published (2015).

[74] J. Hernandez-Rojas, F. Calvo, J. Bretón, and J. M. Gomez Llorente, J. Phys. Chem. C **116**, 17019 (2012).

[75] H. Nada and J. P. J. M. van der Eerden, J. Chem. Phys. **118**, 7401 (2003).

[76] C. Vega, E. Sanz, and J. L. F. Abascal, J. Chem. Phys. **122**, 114507 (2005).

| CNT | temperatures (K) |
|---|---|
| (5,5) | 200 234 274 320 375 438 513 600 |
| (6,6) | 200 226 255 288 326 368 416 470 531 600 |
| (7,7) | 200 213 226 240 255 271 288 307 326 346 368 391 416 442 470 499 531 564 600 |
| (8,8) | 200 213 226 240 255 271 288 307 326 346 368 390 410 430 450 470 485 500 515 530 550 577 600 |
| (9,9) | 200 209 218 228 238 249 260 272 284 297 310 324 339 346 354 358 362 370 382 400 420 440 465 490 515 540 570 600 |
| (10,10) | 200 207 215 222 230 239 247 256 265 275 280 285 290 295 306 317 328 340 352 365 378 392 406 421 436 451 468 485 502 520 539 558 578 600 |

TABLE I. Temperature distributions used in REMD simulations for water inside different (armchair) CNTs with chiral indices $(n, n)$. Every REMD simulation time is 20 ns long.

| CNT | $d$ | $N_W$ | CNT | $d$ | $N_W$ | CNT | $d$ | $N_W$ |
|---|---|---|---|---|---|---|---|---|
| (4,4) | 0.54 | 0 | (8,8) | 1.08 | 17.2 | (20,0) | 1.56 | 39.7 |
| (8,0) | 0.63 | 0 | (14,0) | 1.10 | 17.3 | (12,12) | 1.63 | 44.3 |
| (5,5) | 0.68 | 3.6 | (15,0) | 1.17 | 20.3 | (13,13) | 1.76 | 54.2 |
| (9,0) | 0.70 | 3.6 | (9,9) | 1.22 | 20.9 | (14,14) | 1.90 | 64.5 |
| (10,0) | 0.78 | 3.7 | (16,0) | 1.25 | 23.8 | (15,15) | 2.03 | 76.7 |
| (6,6) | 0.81 | 3.9 | (17,0) | 1.33 | 26.2 | (16,16) | 2.17 | 89.2 |
| (11,0) | 0.86 | 4.5 | (10,10) | 1.35 | 27.6 | (17,17) | 2.30 | 102.7 |
| (12,0) | 0.94 | 10.3 | (18,0) | 1.41 | 29.9 | (18,18) | 2.44 | 117.7 |
| (7,7) | 0.95 | 10.3 | (19,0) | 1.49 | 34.2 | (19,19) | 2.57 | 133.0 |
| (13,0) | 1.02 | 13.9 | (11,11) | 1.49 | 34.7 | (20,20) | 2.71 | 148.9 |

TABLE II. Water occupancy of different armchair $(n, n)$ and zigzag $(n, 0)$ CNTs with diameters $d$ (in nm) for $T = 300$ K, $P = 10^5$ Pa, $\eta = 1$ kJ/mol, and $\delta = 1$ and for the TIP5P water model. Here, $N_W$ denotes the number of water molecules per unit length of 1 nm.

| | CNT | INT | orientation | $\mu$ | $E_{\mathrm{W-W}}$ | $E_{\mathrm{W-C}}$ |
|---|---|---|---|---|---|---|
| A | (5,5) | n.a. | 1:0 | 0.94 | -21.22 | -36.83 |
| A* | (6,6) | n.a. | 1:0 | 0.86 | -25.94 | -27.13 |
| B | (7,7) | $\langle 3,1\rangle$ | 3:0 | 0.91 | -35.02 | -21.34 |
| C | (8,8) | $\langle 5,0\rangle$ | 3:2 uddud | 0.18 | -40.30 | -18.39 |
| D | (8,8) | $\langle 5,0\rangle$ | 4:1 | 0.40 | -41.96 | -18.37 |
| E | (8,8) | $\langle 5,0\rangle$ | 5:0 | 0.64 | -41.41 | -18.36 |
| F | (8,8) | $\langle 5,1\rangle$ | 5:0 | 0.82 | -42.69 | -18.39 |
| G | (8,8) | $\langle 5,2\rangle$ | 5:0 | 0.93 | -41.41 | -18.36 |
| $H_1$ | (9,9) | $\langle 6,0\rangle$ | 3:3 uuuddd | 0 | n.a. | n.a. |
| $H_2$ | (9,9) | $\langle 6,0\rangle$ | 3:3 uuddud | 0 | n.a. | n.a. |
| $I_1$ | (9,9) | $\langle 6,0\rangle$ | 4:2 uuduud | 0.22 | n.a. | n.a. |
| $I_2$ | (9,9) | $\langle 6,0\rangle$ | 4:2 uuuudd | 0.22 | n.a. | n.a. |
| $I_3$ | (9,9) | $\langle 6,0\rangle$ | 4:2 uduuud | 0.22 | n.a. | n.a. |
| J | (9,9) | $\langle 6,0\rangle$ | 5:1 | 0.44 | -41.97 | -15.75 |
| K | (9,9) | $\langle 6,0\rangle$ | 6:0 | 0.65 | -41.97 | -15.75 |
| L | (9,9) | $\langle 6,1\rangle$ | 6:0 | 0.79 | -41.97 | -15.75 |
| M | (10,10) | $\langle 8,0\rangle$ | 4:4 uddduuud | 0 | -40.27 | -15.35 |
| N | (10,10) | $\langle 8,0\rangle$ | 5:3 uuuddddd | 0.16 | -40.56 | -15.33 |
| O | (10,10) | $\langle 8,0\rangle$ | 6:2 udddddud | 0.42 | -40.35 | -15.35 |
| P | (10,10) | $\langle 8,0\rangle$ | 7:1 | 0.51 | -40.33 | -15.37 |
| Q | (10,10) | $\langle 8,0\rangle$ | 8:0 | 0.66 | -40.33 | -15.33 |
| R | (10,10) | $\langle 8,1\rangle$ | 8:0 | 0.74 | -40.64 | -15.17 |

TABLE III. Different minimum energy water structures $\langle\cdot,\cdot\rangle$ found for water inside different armchair CNTs $(n,n)$, $5 \leq n \leq 10$. The structures are characterized by their water orientations u:d (where u and d stand for "up" and "down") and the resulting average axial dipole moments $\mu$. Finally, $E_{\mathrm{W-W}}$ and $E_{\mathrm{W-C}}$ denote the water–water and water–carbon potential energy per molecule, respectively. Note that these structures are also shown in Figs. 4, 5.

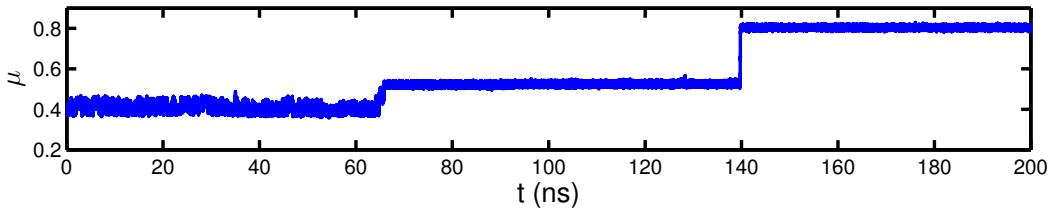


FIG. 1. Time evolution of dimensionless polarization $\mu$ for 177 water molecules inside CNT (8,8) for $T = 300$ K. Note the metastable phases extending over tens of nanoseconds.

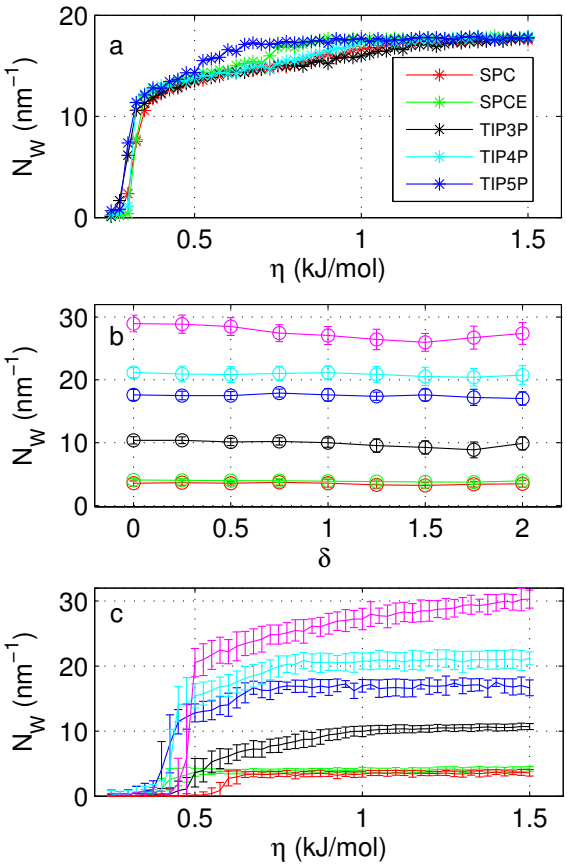


FIG. 2. (a) Influence of water models on water occupancy, $N_W$, inside CNT(8,8), as a function of the water–carbon interaction strength $\eta$, for isotropic interaction, $\delta = 0$. (b) Influence of anisotropy parameter $\delta$ on water occupancy, $N_W$, for fixed water–carbon interaction strength, $\eta = 1$ kJ/mol, and for TIP5P water model. (c) Influence of interaction strength $\eta$ on water occupancy $N_W$, for fixed anisotropy, $\delta = 1$, and for TIP5P water model. Red, green, black, blue, cyan, and magenta curves are for CNT (5,5), CNT (6,6), CNT (7,7), CNT (8,8), CNT (9,9), and CNT (10,10), respectively, in (b) and (c).

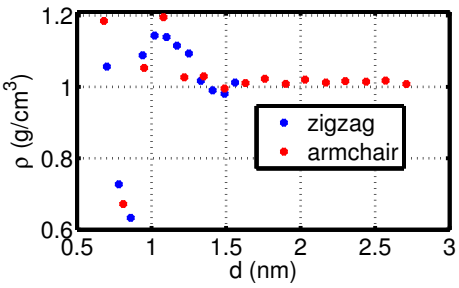


FIG. 3. Water density $\rho = M/V$ versus CNT diameter $d$, for various armchair (red) and zigzag (blue) CNTs for $T = 300$ K, $P = 10^5$ Pa, $\delta = 1$ and $\eta = 1$ kJ/mol and for the TIP5P water model. For the underlying water occupancy numbers, $N_W$, see Tab. II. For the calculation of the inner CNT volume $V$, see Eq. (6).

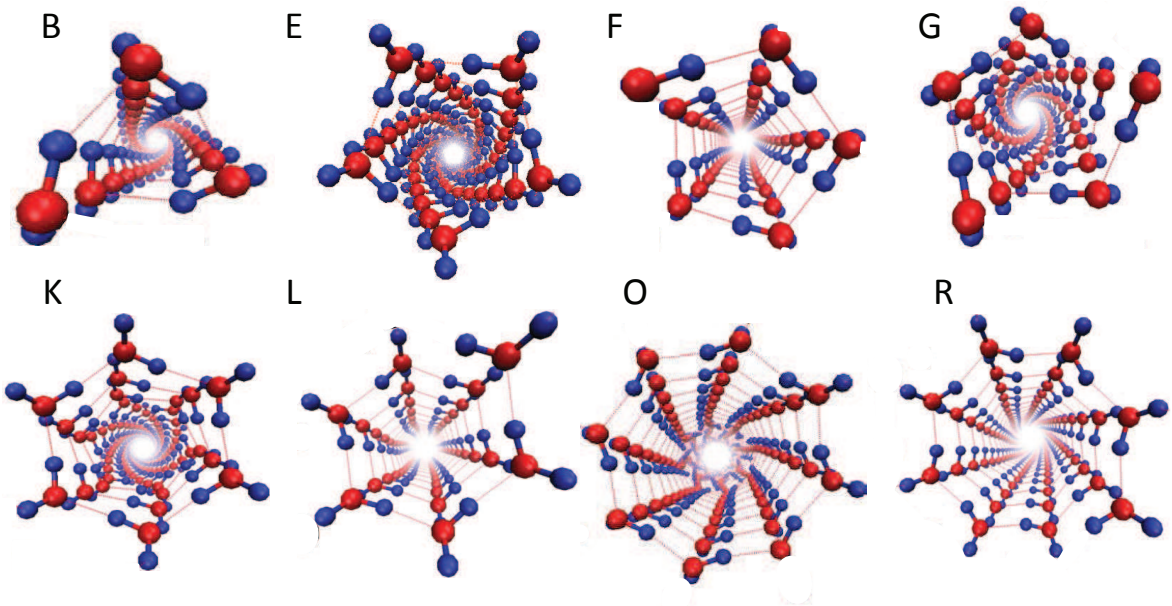


FIG. 4. End views of selected minimum energy structures of INTs confined inside low diameter CNTs. (B): INT $\langle 3,1\rangle$ inside CNT (7,7); (E-G): INT $\langle 5,0\rangle$, $\langle 5,1\rangle$, $\langle 5,2\rangle$ inside CNT (8,8); (K-L): INT $\langle 6,0\rangle$, $\langle 6,1\rangle$ inside CNT (9,9); (O-R): INT $\langle 8,0\rangle$, $\langle 8,1\rangle$ inside CNT (10,10). For more INT structures, see Tab. III and Fig. 5.

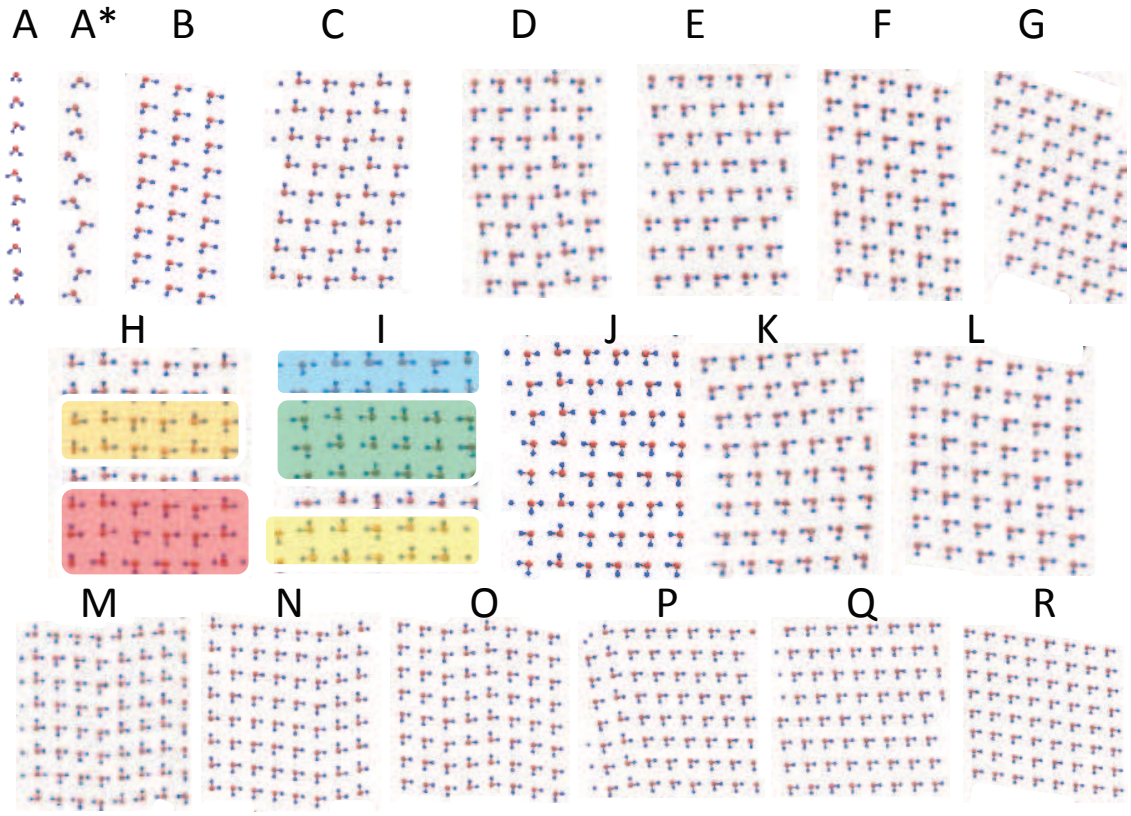


FIG. 5. Unrolled representations of minimum energy structures of water confined inside low diameter CNTs. (A, A*): Water chains inside CNT (5,5) and (6,6); (B): INT $\langle 3, 1\rangle$ inside CNT (7,7); (C-G): INT $\langle 5, \cdot\rangle$ inside CNT (8,8); (H-L): INT $\langle 6, \cdot\rangle$ inside CNT (9,9); (M-R): INT $\langle 8, \cdot\rangle$ inside CNT (10,10). For more detailed informations, see Tab. III.

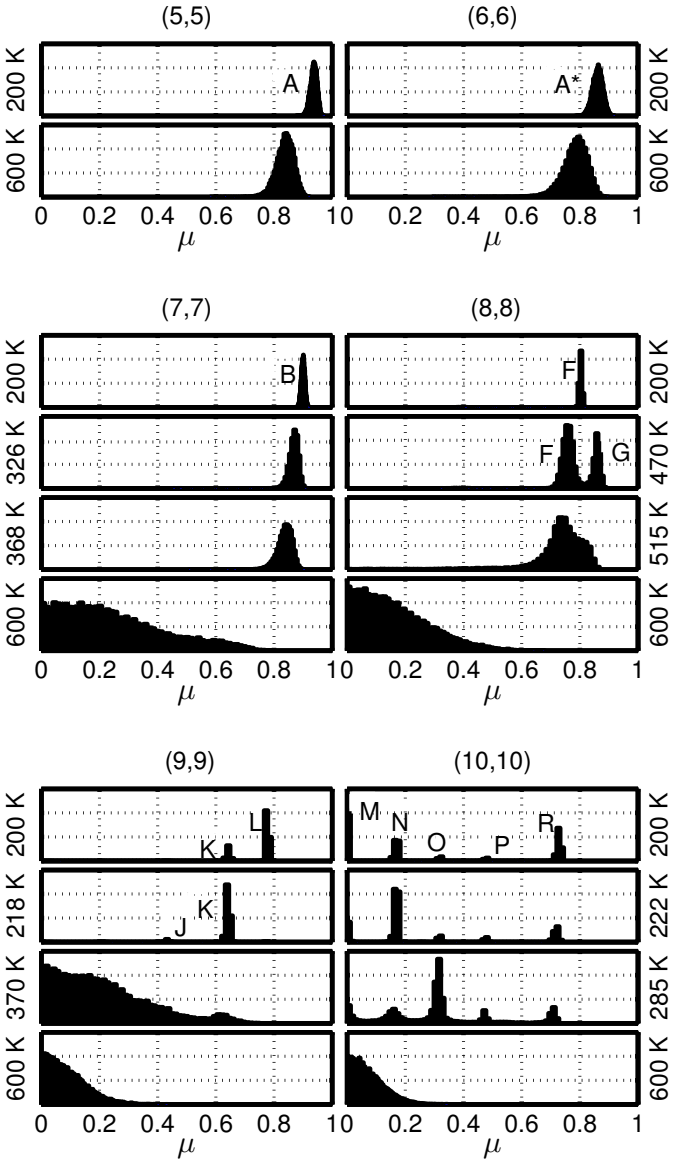


FIG. 6. Histograms of the dimensionless polarization, $\mu$, of water confined inside armchair CNT $(n, n)$, $5 \leq n \leq 10$ for selected temperatures. Obtained from REMD simulations with $\eta = 1$ kJ/mol, $\delta = 1$, and for the TIP5P water model.

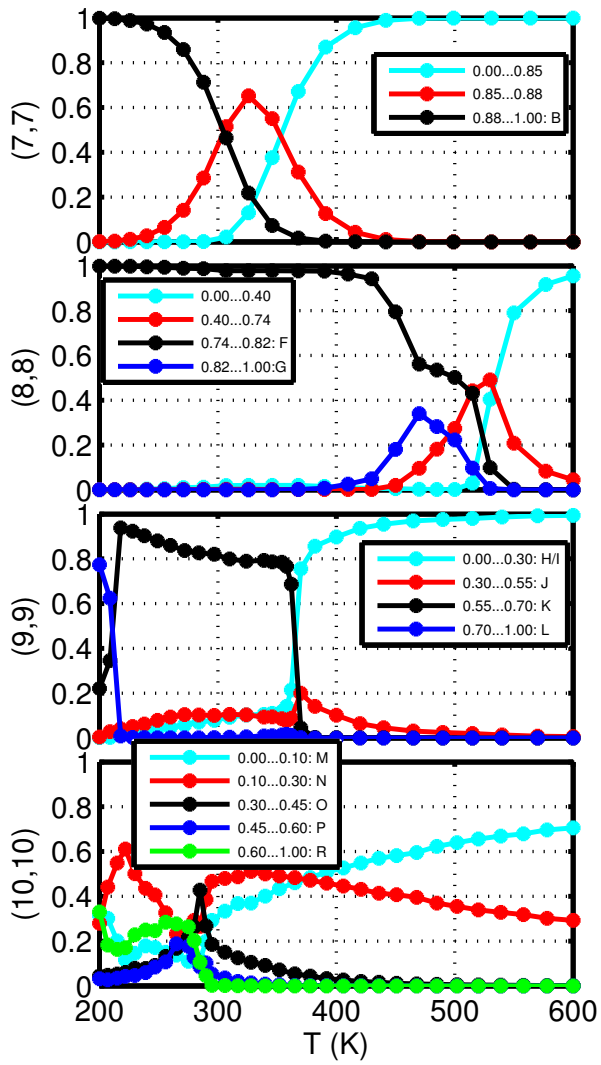


FIG. 7. Populations of different polarization states of water confined inside armchair CNT $(n, n)$, $7 \leq n \leq 10$ as a function of temperature. Obtained from REMD simulations with $\eta = 1$ kJ/mol, $\delta = 1$, and for the TIP5P water model.

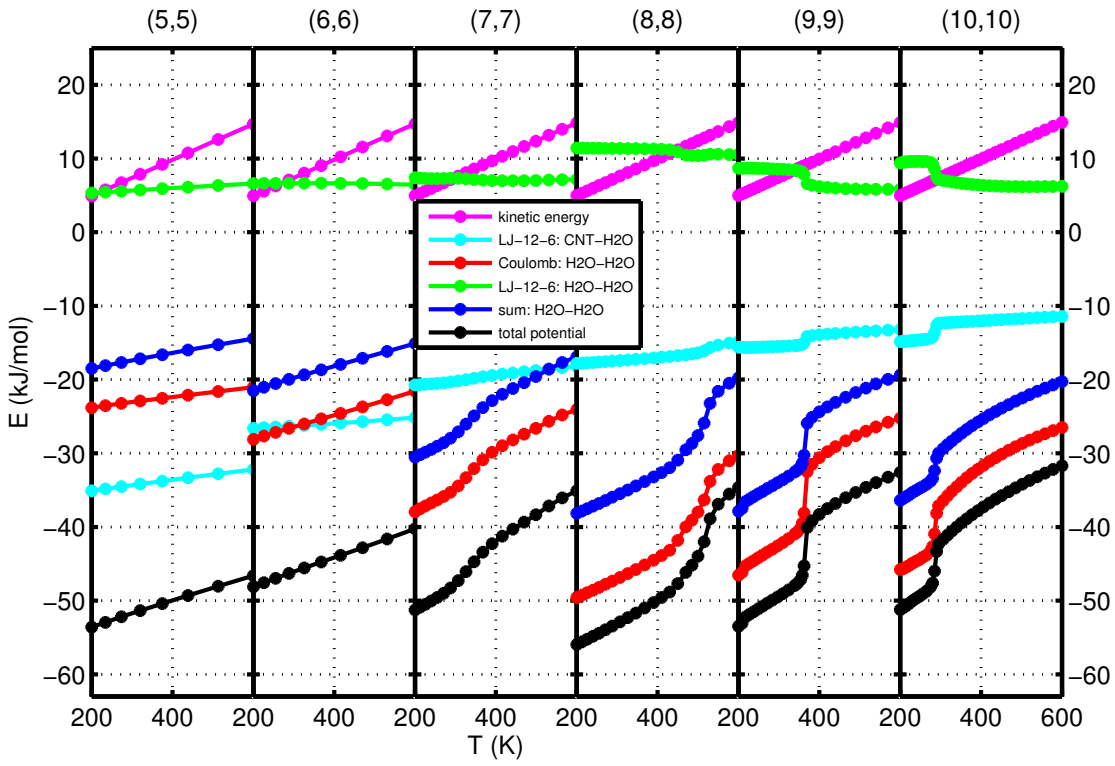


FIG. 8. Decomposition of total energy in REMD simulations of water confined inside armchair CNT $(n, n)$, $5 \leq n \leq 10$ as a function of temperature. For $\eta = 1$ kJ/mol, $\delta = 1$, and for the TIP5P water model.

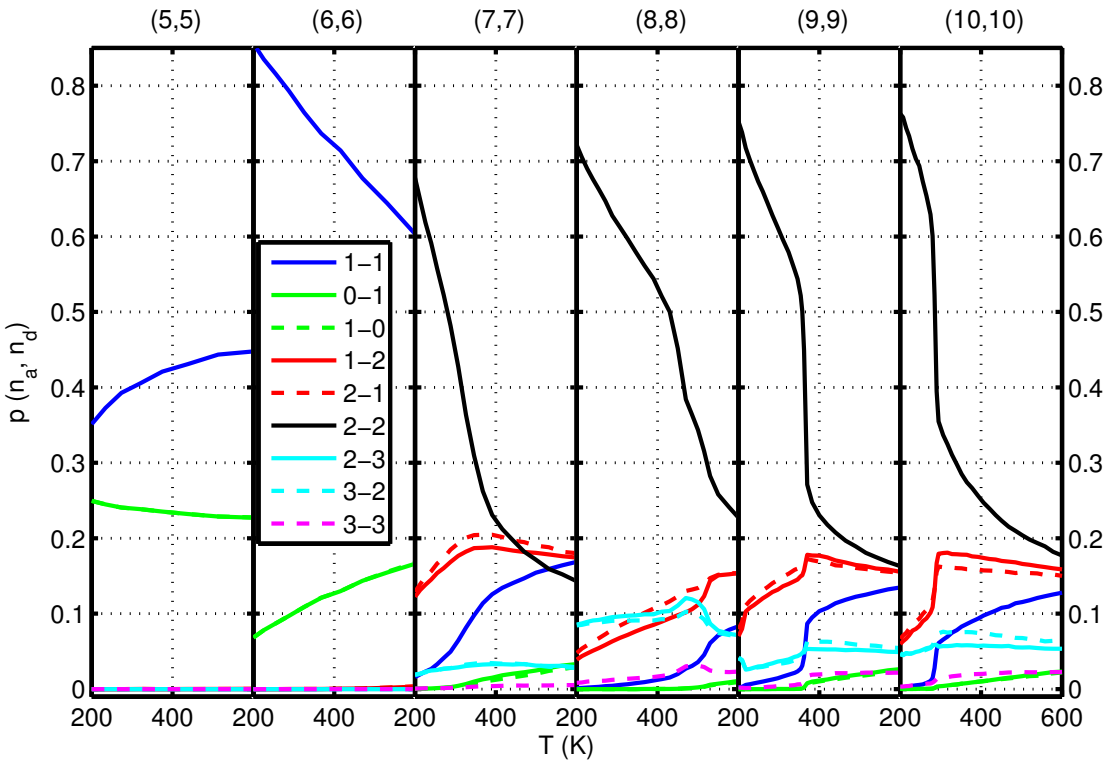


FIG. 9. H–bonding pattern of water confined inside armchair CNT $(n, n)$, $5 \leq n \leq 10$ as a function of temperature. Obtained from REMD simulations with $\eta = 1$ kJ/mol, $\delta = 1$, and for the TIP5P water model. The curves indicate the joint probabilities, $p(n_a, n_d)$, of a water molecule acting $n_a$ times as an acceptor and $n_d$ times as a donor, with indices $(n_a, n_d)$ indicated in the figure legend.